Materials Advances

ROYAL SOCIETY OF CHEMISTRY

PAPER

View Article Online
View Journal | View Issue

Cite this: *Mater. Adv.*, 2024, 5, 719

Synthesis of FeCoNiCuPt high-entropy alloy nanoparticle electrocatalysts with various Pt contents by a solid-state reaction method

Chao Meng,[a] Xuhui Wang,[ab] Zhiyong Li,[ab] Chun Wu, *[abcd] Ling Chang,[c] Runqing Liu[d] and Wenli Pei *[c]

Received 11th October 2023,
Accepted 3rd December 2023

DOI: 10.1039/d3ma00834g

rsc.li/materials-advances

FeCoNiCuPt high-entropy alloy nanoparticles with small sizes (3–7 nm) and different Pt contents have been successfully synthesized by a facile solid-state reaction method. The exposed surface absorption or oxidation of Fe, Co, Ni, and Cu elements; the centered diffraction angles of a single solid solution phase; and the uniform element distributions in nanoparticles illustrate the high-entropy characteristic of nanoparticles. The lattice parameters and grain sizes of nanoparticles are increased by increasing the Pt content from 10% to 30%. The C_{dl} and ESCA of FeCoNiCuPt nanoparticles are higher than that of commercial Pt/C when the Pt contents are 20% and 30%. The maximum HER/MOR activities and long-term stability of FeCoNiCuPt nanoparticles are achieved when the Pt content is 20%. DFT calculations reveal that the biggest d-orbital overlap bandwidth and the strongest coordinate effects of each element in FeCoNiCuPt nanoparticles are obtained when the Pt content is 20%, which leads to the enhancement of electrocatalytic properties. Thus, this work provides a feasible strategy for synthesizing Pt-based high-entropy alloy nanoparticle electrocatalysts.

1. Introduction

Alloying Pt with relatively higher abundance elements (such as Fe, Co, Ni, and Cu) is one of the most effective strategy to reduce the cost of commercial Pt/C catalysts, which also improves the electrocatalytic performance of Pt-based alloys.[1–3] The preparation and application of Pt-based binary or ternary alloys have already been widely studied.[1–7] With the increase in element types in Pt-based alloy catalysts, the high-entropy alloy (HEA) with at least five kinds of elements and an entropy higher than 1.5*R* has received extensive attention in recent years.[8–11] Typically, the small-sized FeCoNiCuPt HEA nanoparticle (NP) synthesized by a low-temperature oil phase method presents a very small overpotential of 11 mV, which is only about 13% of commercial Pt/C catalysts, the mass activity for an HER and MOR can be enhanced to achieve 13.20 and 10.37 times higher activity.[12] The NiCuPdAgPt HEA obtained by a surfactant-free synthesis strategy showed a positive cocktail effect, which greatly enhanced the MOR performance to 1.2 times higher than that of Pt/C. The ultrafine FeCoNiCuPt HEA NPs prepared by the impregnation reduction method displayed a significant specific activity (2.5 times of Pt/C) and CO tolerance to MOR.[13,14] The ultra-small FeCoNiRhPt and FeCoNiTaPt HEA NPs used for acidic water splitting also showed an excellent activity and stability at a high current density.[15,16] The irreplaceable advantages of Pt-based HEA NPs for electrocatalysis can be summarized as follows. Firstly, the Pt dosage in HEA NPs will be greatly reduced with increasing element types. Secondly, the thermal stability of HEA NPs can be enhanced by increasing the entropy value, which ensures durability in the electrocatalytic process because the alloy elements in HEA NPs are hard to etch.[11–16] Thirdly, as the atomic size differences induce stress and interaction between elements, the d-band center of Pt can be lowered by alloying with suitable elements, which further improves the electrocatalytic activity.[17] In addition, the multi-component can act as an active multi-site in electrocatalysis and will correspondingly tune the multielectron transfer processes; the so-called cocktail effect will create a fast site-to-site electron transfer route, which improves both the electrocatalytic selectivity and activity.[8–12] Therefore, researchers commonly aim to discover highly efficient Pt-based HEA catalysts.

The electrocatalytic properties of Pt-based HEA NPs are highly related to the composition and microstructure, smaller size, and tunable components are two important characteristics of highly efficient Pt-based HEA NPs catalysts.[15–18] Grain refinement of catalysts will increase the specific surface area, and the activity of active sites on the surface increases accordingly, which

[a] *School of Materials Science and Engineering, Liaoning Technical University, Fuxin, 123000, China. E-mail: chun_wu@126.com*
[b] *Ordos Institute of Liaoning Technical University, Ordos, 017010, China*
[c] *Key Laboratory of Anisotropy and Texture of Materials (Ministry of Education), Northeastern University, Shenyang, 110819, China. E-mail: peiwl@atm.neu.edu.cn*
[d] *Science and Technology Development Corporation, Shenyang Ligong University, Shenyang, 110159, China*

maximizes Pt utilization and boosts mass transfer in the electrocatalytic process. However, if the NPs are too small, the exposed crystal faces will change, and the NPs will be easily dissolved. The activity and selectivity of catalysts always show volcano trends with respect to the sizes; some studies suggest that the optimal size of Pt-based catalysts should at least be less than 6 nm.[19,20] The selection of components in Pt-based HEA NPs is not only related to the abundance but also depends on the function of elements. The magnetic elements (Fe, Co, Ni, *etc.*) can be employed to enhance the magnetic property of NPs, which facilitates the adsorption of magnetic intermediates and improves electrocatalytic kinetics.[21,22] The antioxidant elements (Cu, Zn, *etc.*) will prevent the oxidation and dissolution of NPs, which enhances the long-term stability of the catalyst.[1,23] Selection of competitive elements in Pt-based HEA is essential for improving its electrocatalytic performance; meanwhile, the content of component elements should not be ignored, especially for the most expensive element Pt, which contributes the most to the electrocatalysis process. Optimizing the content of Pt in HEA NPs will not only reduce the cost of the catalyst but also stimulate the cocktail effect of each element to improve the electrocatalytic kinetics.

To optimize the Pt content in HEA NPs, the FeCoNiCuPt HEA contains both higher abundance and functional elements selected as the model catalyst, and the DFT calculation method is employed to illustrate the multi-component cocktail effect. The Pt content in HEA NPs is carefully controlled to 10%, 20%, and 30%, and the proportions of other elements are kept equal to insurance the entropy of HEA NPs (larger than 1.5R). To prepare the HEA NPs with smaller size (less than 6 nm) and uniform solid solution phase, an insulating medium-assisted solid-state reaction method has been employed, which presents the advantages of surfactants-free, higher precursors utilization rate, and can be used to synthesize ultra-small size Pt-based alloy NPs with thermal stable phase.[24–28] In addition, the effects of Pt content on the microstructure and electrocatalytic properties of FeCoNiCuPt HEA NPs have been studied in this research.

2. Research methods

2.1 Synthesis of FeCoNiCuPt HEA NPs

FeCoNiCuPt HEA NPs were synthesized by a medium-assisted solid-state reaction method, as shown in Fig. 1. Firstly, mixing of the precursor solution and solid-state isolating medium was done. Iron acetylacetonate ($Fe(acac)_3$), nickel acetylacetonate ($Ni(acac)_2$), platinum acetylacetonate ($Pt(acac)_2$), copper acetate ($Cu(ac)_2$), and cobalt acetylacetonate ($Co(acac)_3$) precursors with different proportions were dissolved in hexane and ethanol at 50 °C by continued stirring until creating a uniform precursor solution. The NaCl powder was employed as the solid isolating medium, which was ground to a size of less than 9 ± 1 μm. NaCl powders with a mass about 300 times that of the precursors were added to the precursor solution, and the mixed solution was dried slowly at 80 °C. Then, the solid-state reaction of the mixture was carried out. The obtained NaCl–precursors mixture powders were moved to a tube furnace filled with a reducing atmosphere (90% Ar + 10% H_2). The mixed powders were heated to 600 °C at a rate of 10 °C min^{-1} and held for 180 minutes. Finally, the purification and enrichment of NPs was done. After cooling down to room temperature, the black mixed powders were dissolved into a large amount of deionized water. The HEA NP was collected by centrifugation several times with ethanol and stored in ethanol at −20 °C. To synthesize FeCoNiCuPt HEA NPs with different Pt contents, the total amounts of precursors were kept constant at 1 mmol, the amounts of Fe, Co, Ni, and Cu precursors were in equimolar ratio, the Pt precursors amount was selected as 0.1, 0.2, and 0.3 mmol, and the aimed Pt content in HEA NPs were controlled at 10%, 20%, and 30%.

2.2 Microstructure and properties detection of FeCoNiCuPt HEA NPs

An energy dispersive spectrometer (EDS, XFlash 5030T, Bruker, Germany), inductively coupled plasma-mass spectrometer (ICP-MS, Agilent 7800), and X-ray photoelectron spectrometer (XPS, Thermo VG, ESCALAB250, America) were employed to detect the composition of HEA NPs. Photons were generated by a monochromatized Al Kα X-ray source (1486.6 eV) with 500 mm spot size and 50 eV pass energy at 12 kV. The surface contamination C 1s was calibrated to 284.8 eV with the FWHM range of 0.8–1.2 eV. The Cu Kα X-ray diffraction (XRD) detection was used for detecting the crystal structure of HEA NPs, which was performed on a Rigaku D/Max 2400 diffractometer in the 2θ range of 30°–80°. The JEM-2100F field emission transmission electron microscope (TEM) produced by JEOL in Japan was applied to observe the morphology and size of the NPs; a high-resolution transmission electron microscope (HRTEM) was

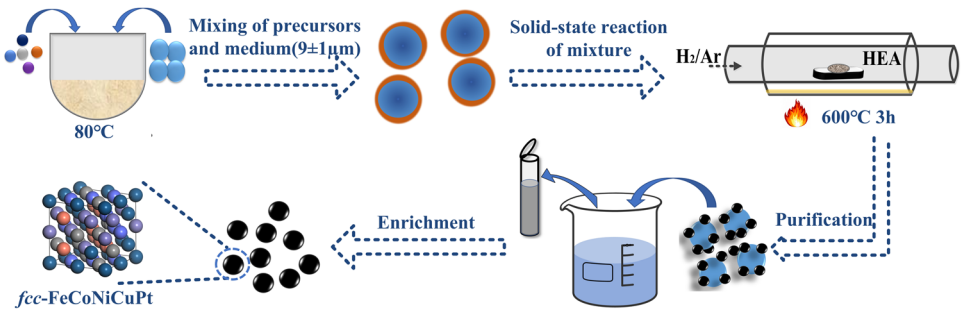

Fig. 1 Preparation procedures of FeCoNiCuPt HEA NPs by the solid-state reaction method.

used to analyze the interplanar spacing, and the diffraction rings were collected by selected area electron diffraction (SAED). Diameters more than 100 NPs in the TEM images were counted as the characteristic grain size.

The electrochemical properties were tested on a CS235OH electrochemical workstation through a three-electrode system in 1 M KOH and 1 M KOH + 1 M CH_3OH electrolyte. The counter electrode was a carbon rod, the reference electrode was a mercury oxide electrode, and the working electrode was a 3 mm diameter glassy carbon electrode loaded with HEA NPs. About 2 mg HEA NPs were dispersed in 196 μL isopropanol and 4 μL Nafion solution and ultrasonicated for 45 minutes until the NPs were uniformly dispersed in the solution. Then, 7 μL solution was dropped on the glassy carbon electrode, and the catalyst loading mass on glassy carbon was about 1 mg cm^{-2}. The polarization curve (LSV) was tested in 1 M KOH alkaline medium at a scanning speed of 5 mV s^{-1}. As the high electrolyte concentration in test, the *iR* correction was not performed. The double layer capacitance (C_{dl}) of NPs was tested by cyclic voltammetry from 0.38 to 0.48 V at a scanning rate of 25–125 mV s^{-1}. The electrochemical surface area (ECSA) was evaluated by ECSA = C_{dl}/C_s, where C_s = 0.04 mF cm^{-2} is the general specific capacitance. Electrochemical impedance spectra (EIS) were measured at a current density of 10 mA cm^{-2}, the frequency ranged from 0.1 to 100 kHz. Cyclic voltammetry (CV) was used to study the MOR performance in 1 M KOH + 1 M CH_3OH solution. The MOR activity was measured at a scan rate of 50 mV s^{-1} in the same potential range, and the initial potential and peak current were compared. The long-term stability of the HEA NPs was evaluated by monitoring the overpotential at a current density of 10 mA cm^{-2} for about 10 hours.

2.3 Theoretical calculation of FeCoNiCuPt HEA NPs

All static calculations in this paper were performed using density functional theory (DFT) and VASP 5.4.4 (Vienna *ab initio* simulation package). The generalized gradient approximation (GGA) PBE (Perdew Burke Ernzerhof exchange–correlation) was used to calculate the exchange–correlation energy. The cutoff energy of the plane wave basis was set as 500 eV, and the Brillouin zone integral was optimized by a 5 × 5 × 1 *k* grid. The atomic position and horizontal lattice parameters were optimized by the conjugate gradient algorithm. The convergence criteria of energy and force were set to 1.0×10^{-6} eV and −0.01 eV $Å^{-1}$, respectively. The calculation model was the (111) face of HEA NPs with a face-centered cubic (fcc) structure. In order to balance the difficulty of calculations with the comparability of the models to the experimental results, the atom ratios of (Fe + Co + Ni + Cu) : Pt were set as 9 : 1, 8 : 2, and 7 : 3, in which the Fe, Co, Ni, and Cu atoms were in equal proportion.

3. Results and discussion

3.1 Microstructure of FeCoNiCuPt HEA NPs

The contents of each element in FeCoNiCuPt HEA NPs are summarized in Fig. 2. The composition of HEA NPs was

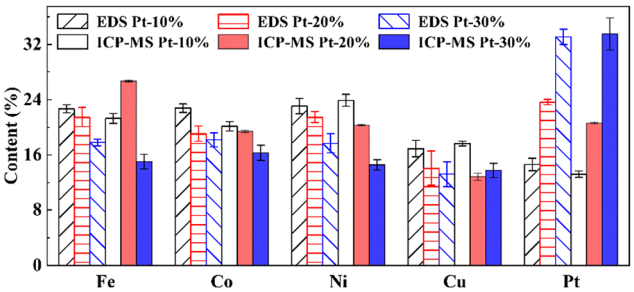

Fig. 2 The composition of FeCoNiCuPt HEA NPs.

detected as $Fe_{22.7}Co_{22.8}Ni_{23.1}Cu_{16.9}Pt_{14.6}$, $Fe_{21.5}Co_{19.1}Ni_{21.5}Cu_{14.1}Pt_{23.7}$, and $Fe_{17.8}Co_{18.2}Ni_{17.7}Cu_{13.2}Pt_{33.1}$ when the Pt precursors amount was 10%, 20%, and 30%, in which the differences between EDS and ICP-MS results are less than 2.7%. The actual content of Fe, Co, and Ni elements are similar to the nominal content. However, the Cu content is slightly lower and the Pt content is higher (less than 4.5%). It is still unclear why the Cu contents in NPs are lower than expected: one possible reason is that some Cu precursors ($Cu(ac)_2$) may react with NaCl powders to create the water-soluble salts (such as $CuCl_2$) in the high-temperature solid-state reaction process, which are dissolved by water when collecting the NPs by washing and centrifugation. Although the solid-state reaction method can be employed to enhance the utilization rates of precursors,[24–27] suitable metal precursors are still necessary for synthesizing the HEA NPs.

The XPS patterns of NaCl–precursors mixture powders before solid-state reaction and the as-synthesized HEA NPs when using 20% Pt precursors amounts are shown in Fig. 3(a)–(f). The Fe 2p, Co 2p, Ni 2p, and Cu 2p spectra consist of $2p_{1/2}$, $2p_{3/2}$, and their satellite peaks, while the Pt 4f spectrum contains $4f_{5/2}$ and $4f_{7/2}$ peaks. The NaCl powders and precursor solution were mixed by slowly stirring and drying. In this process, the charges of Cu^{2+}, Ni^{2+}, and Pt^{2+} are the same as the raw metal precursors, but some low-charged Fe^{2+} and Co^{2+} ions are generated. The ratios of Fe, Co, Ni, Cu, and Pt ions in the mixture powders are nearly equal, which agrees well with the proportion of precursors. The mixing of NaCl powders and precursor solution will not lose the precursors but will lower the charge of Fe^{3+} and Co^{3+}. The XPS patterns of the as-synthesized NPs shows the presence of metal atoms and ions. The spectra of Fe, Co, Ni, and Cu elements contain pure atoms with a charge of 0 and ions with a charge of 2^+. However, the spectra of the Pt element contain only the atoms with a charge of 0 because the Pt element is hard to be oxidized when compared with the Fe, Co, Ni, and Cu elements. The peak position of Pt $4f_{5/2}$ is located at about 73.0 eV and lower than some standard Pt^0 (about 74.8 eV), which indicates the alloying of Pt with other elements. The absorption of H_2O, O_2, and the surface oxidation of NPs in the purification and collection process will generate some 2^+ metal ions in the surface layers of HEA NPs. Otherwise, the binding energies of Fe, Co, Ni, and Cu ions with a charge of 2^+ in HEA NPs are higher than that in NaCl–precursors mixture powders because the binding energy of oxide is higher than that of precursors (acetylacetone or acetate compounds), which also illustrates the thermal

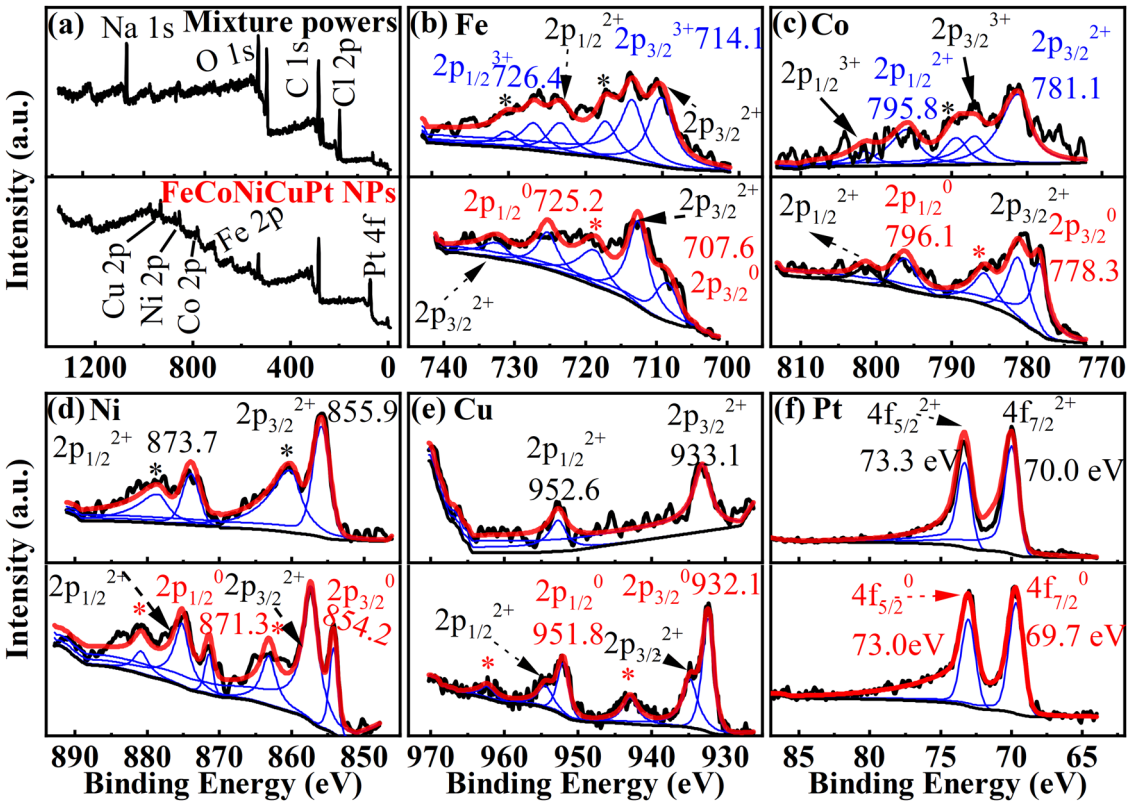

Fig. 3 XPS spectra of NaCl–precursor mixture powders and HEA NPs. (a) Full spectra, (b) Fe 2p, (c) Co 2p, (d) Ni 2p, (e) Cu 2p, and (f) Pt 4f.

decomposition of precursors in the solid-state reaction process. It must be noted that the oxides of Fe, Co, Ni, and Cu elements exist simultaneously on the surface of HEA NPs, which suggests that the elements in HEA NPs are evenly distributed without segregation.

Fig. 4(a) is the XRD patterns of FeCoNiCuPt HEA NPs with different Pt contents. Three diffraction peaks of NPs can be observed; they are located at about 43°, 50°, and 72° and can be indexed to the (111), (200), and (220) faces of the solid solution phase with the fcc structure, respectively. It must be noted that the diffraction angles of HEA-(111) peaks are located between Pt-(111) and Fe/Co/Ni/Cu-(111), which is caused by the alloying of Fe, Co, Ni, Cu, and Pt atoms in NPs. With the increase in the Pt content, the diffraction peaks of HEA NPs shift to the left side. The lattice parameter a of HEA NPs was calculated using the diffraction angles corresponding to the (111) and (200) peaks. As shown in the inset in Fig. 4(b), the lattice parameter a of HEA gradually increases with increasing Pt content; because the atomic radius of Pt is larger than that of Fe/Co/Ni/Cu, more Pt content in NPs means larger lattice parameters

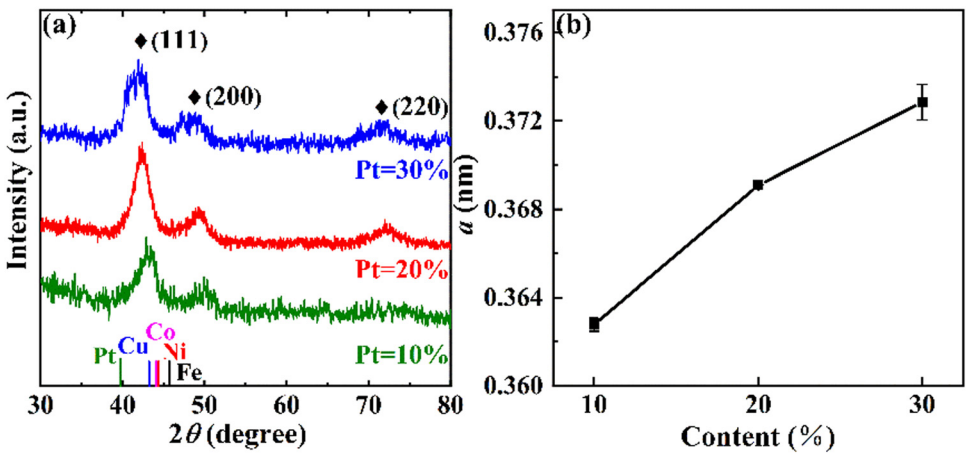

Fig. 4 XRD patterns (a) and lattice parameter a (b) of FeCoNiCuPt HEA NPs with different Pt contents.

and lower diffraction angles. The formation of a single solid solution phase, diffraction angles of HEA-(111) peaks, and the evolution of lattice parameters illustrate that the HEA NPs are obtained by the solid-state reaction method.[29–31]

Fig. 5(a)–(c) show the TEM images of FeCoNiCuPt HEA NPs. The morphology of HEA NPs is uniform spherical, and no obviously abnormal sintering can be found. The HRTEM images of 20% and 30% Pt content HEA NPs are shown in Fig. 5(b1) and (c1). The lattice fringes in the images are parallel to each other; the uniform lattice fringes indicate they are monocrystalline NPs. The lattice spacing of 0.210 and 0.213 nm corresponded to the (111) faces of fcc structure. The SAED rings of the 20% and 30% Pt content HEA NPs are shown in Fig. 5(d1) and (d2); the rings can be indexed as the (111), (200), and (220) faces of the fcc structure. The element distributions of an HEA NP with Pt contents of 20% are shown in Fig. 5(e). The Fe, Co, Ni, Cu, and Pt elements are nearly uniformly distributed in the NP, which indicates the alloying of Fe, Co, Ni, Cu, and Pt elements in HEA NPs. The higher solid-state reaction temperature (600 °C) facilitates the formation of a solid solution phase, which is consistent with the XPS and XRD results.

The minimum diameter is treated as the characteristic size of a FeCoNiCuPt HEA NP, and the size distributions are shown in Fig. 5(f). The size distributions are fitted well with the single-peak Gauss function, which reveals the typical ripening growth behavior of HEA NPs; the NPs are hard to attach as the resistance of the solid isolating medium.[24–27] The sizes of most HEA NPs are located in the range from 3 to 7 nm, and the contents of NPs with size higher than 7 nm are less than 20%. The Pt-based catalysts in this smaller region always present excellent electrocatalytic performance.[19,20,32,33] The size distributions of HEA NPs move to the right side with increasing Pt content, which means that the average size of HEA NPs is positively correlated with the Pt content. In view of the growth process, the growth rates of HEA NPs on the solid isolating medium are the same because the diffusion-growth temperature, time, interface areas, and the total amount of precursors are consistent in the solid-reaction process.[25–27] Thus, it can be deduced that increasing the Pt precursor amount may decrease the nucleation ratio of HEA NPs. The thermal decomposition temperature of Pt precursors is higher than that of Fe, Co, Ni, and Cu.[27,33] The total amount of precursors remains unchanged in the solid-reaction process, and the concentration

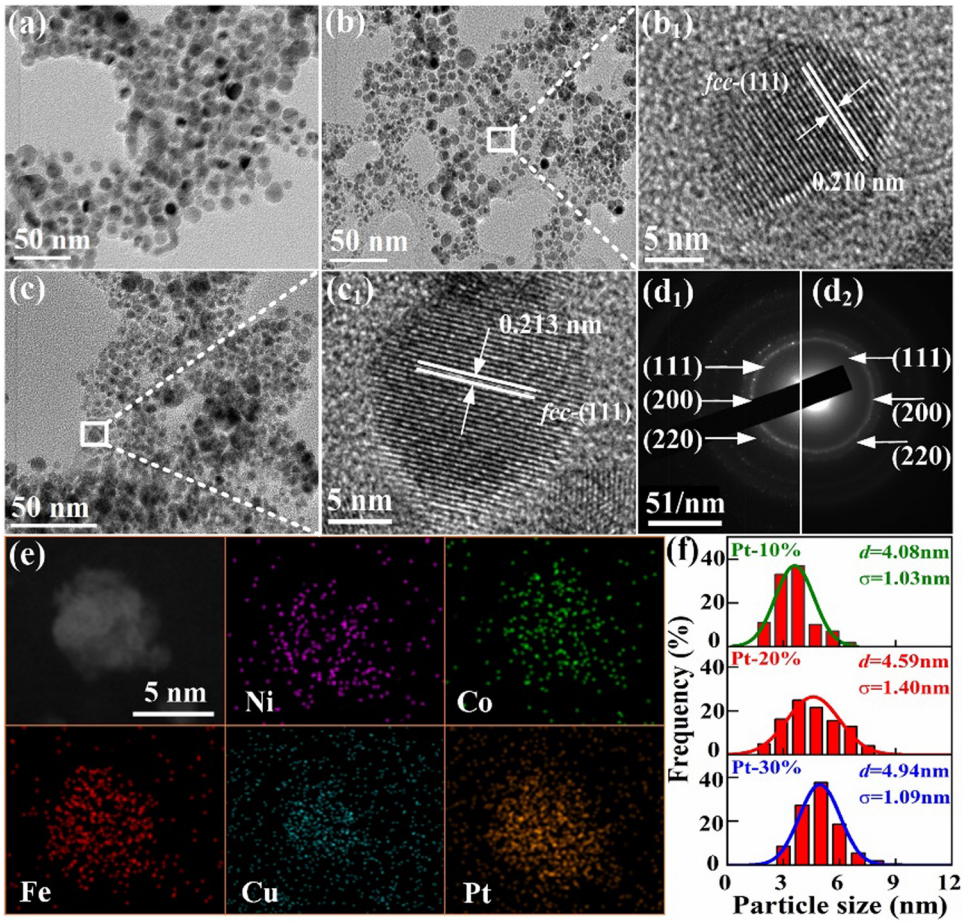

Fig. 5 TEM images of FeCoNiCuPt HEA NPs with Pt contents of (a) 10%, (b) 20%, and (c) 30%. HRTEM images of NPs with Pt contents of (b_1) 20% and (c_1) 30%. SAED images of NPs with Pt contents of (d_1) 20% and (d_2) 30%. (e) Elemental mapping of HEA NPs with Pt contents of 20%. (f) Grain size distributions of HEA NPs.

of precursors decomposed preferentially (Fe, Co, Ni, and Cu) in the nucleation stage decreases with increasing Pt content, which leads to the decrease in the nucleation ratios and the increase in grain size. Nevertheless, the FeCoNiCuPt HEA NPs with uniform size distributions, smaller size, and high-entropy solid solution phase are successfully prepared by the NaCl-assisted solid-state reaction method.

3.2 Electrochemical properties of FeCoNiCuPt HEA NPs

Fig. 6(a) shows the electrochemical double layer current (*i vs.* scan rate) of FeCoNiCuPt HEA NPs, which was obtained from the CV data collected at a scan rate of 25–125 mV s^{-1}. Compared with the commercial Pt/C (31.8 mF) catalyst, the C_{dl} of HEA NPs becomes larger when the Pt content is higher than 20%. However, further increasing the Pt content to 30% decreases the C_{dl}. The C_{dl} reaches the maximum of 85.8 mF when the Pt content is 20%, which means that 20% Pt content HEA NPs expose more active sites for adsorption and desorption.[34–36] The ECSA of FeCoNiCuPt HEA NPs with different Pt contents are obtained from the C_{dl} and shown in Fig. 6(b). The ECSA of 20% and 30% Pt content HEA NPs are 2.70 and 1.09 times that of the commercial Pt/C catalyst, respectively; the maximum ECSA is achieved when the Pt content is 20%.

Fig. 7(a) and (b) show the ECSA and Pt loading normalized HER polarization curves of HEA NPs. The overpotentials of FeCoNiCuPt HEA NPs with different Pt contents at 10 mA cm^{-2} are 174.2, 22.5, and 62.4 mV, respectively. The linear sweep voltammetry (LSV) curve of 20% Pt content FeCoNiCuPt HEA NPs shows a low overpotential of 22.5 mV, which is only about 60.5% that of the commercial Pt/C catalyst (37.2 mV). As shown in Fig. 7(c), the area activity of HEA NPs reaches the maximum of 0.026 mA cm^{-2} and the mass activity reaches 273 mA mg_{pt}^{-1} at −0.07 V. The HEA NP with 20% Pt content presents better HER activities; they are about 1.04 and 2.15 times of the commercial Pt/C catalyst (0.025 mA cm^{-2} and 127 mA mg_{pt}^{-1}), respectively. The Tafel slope is calculated from the LSV curves to illustrate the HER kinetics of HEA NPs. As shown in Fig. 7(d), the Tafel slopes of commercial Pt/C catalysts and FeCoNiCuPt HEA NPs are 40.4, 120.3, 18.7, and 52.2 mV dec^{-1}, respectively. The HER kinetics of Pt/C catalyst follows the Volmer–Heyrovsky process, in which the Heyrovsky reaction is the rate-determining step. When the Pt content in HEA NPs is lower (10%), the rate-determining step of HER is the Volmer reaction, similar to some Pt-free catalysts.[37] The HEA NPs with Pt content of 20% follow the Volmer–Tafel process; the rate-determining step of HER is the Tafel reaction and exhibits a faster rate of HER reaction. Increasing the Pt-content to 30%, the Tafel slope of 52.2 mV dec^{-1} indicates a mixed rate-determining step. In order to further understand the interface reaction in the HER process, electrochemical impedance spectroscopy (EIS) analysis of FeCoNiCuPt HEA NPs was performed. As shown in Fig. 7(e), the FeCoNiCuPt HEA NPs with Pt content of 10% and 20% present a smaller semicircle radius in the Nyquist diagram, which means the smaller charge transfer resistance and faster charge transfer in the surface of NPs.[38–41] The charge transfer resistance of HEA NPs is lower than that of Pt/C, and it increases with the increase in the Pt content. The Tafel slope of HEA NPs with 20% Pt content is lower than that of 10%, but the charge transfer resistance is slightly higher. Although the specific reason is not clear, a possible reason is that the grain size of 10% Pt content HEA NPs is smaller, which always presents the ability to lower the charge transfer resistance.[30] Fig. 7(f) shows the chronocurrent curves of FeCoNiCuPt HEA NPs in 1 M KOH at a current density of 10 mA cm^{-2}. After discharge for 30 000 s, the 20% Pt content HEA NPs still maintain 94.5% of the current density, which is much better than the commercial Pt/C catalyst (82.3%), but the FeCoNiCuPt HEA NPs with 10% and 30% Pt content can only maintain 72.3% and 56.7% of the catalytic activity. The corrosion resistance of Fe, Co, Ni, and Cu atoms is weaker than Pt; they are more easily dissolved and precipitated in the HER electrocatalytic process. The formation of a thermodynamics stable phase is essential for improving the stability of FeCoNiCuPt HEA NPs. The FeCoNiCuPt HEA NPs with different Pt content show a similar solid solution phase with the fcc structure; however, the entropy value of HEA NPs is quite different. The actual entropies of 10%, 20%, and 30% Pt content HEA NPs are 1.59, 1.60, and 1.55*R* (according to the composition), respectively.

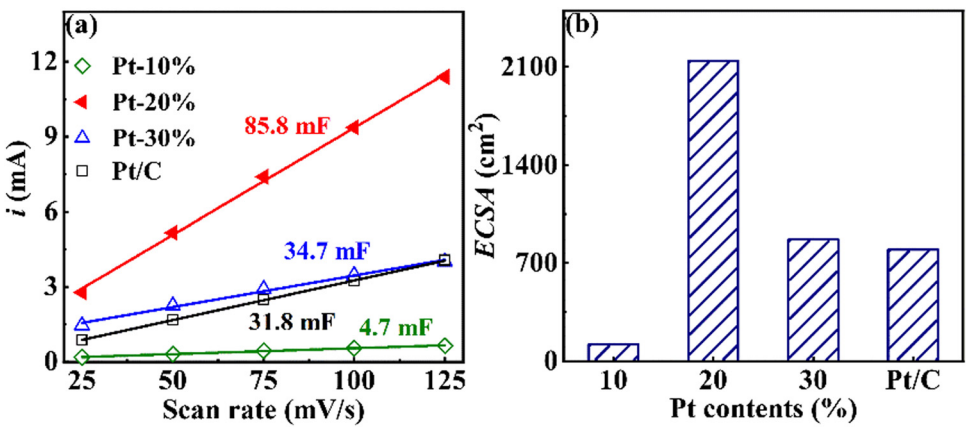

Fig. 6 Electrochemical double layer capacitance (a) and ECSA (b) of FeCoNiCuPt HEA NPs with different Pt contents.

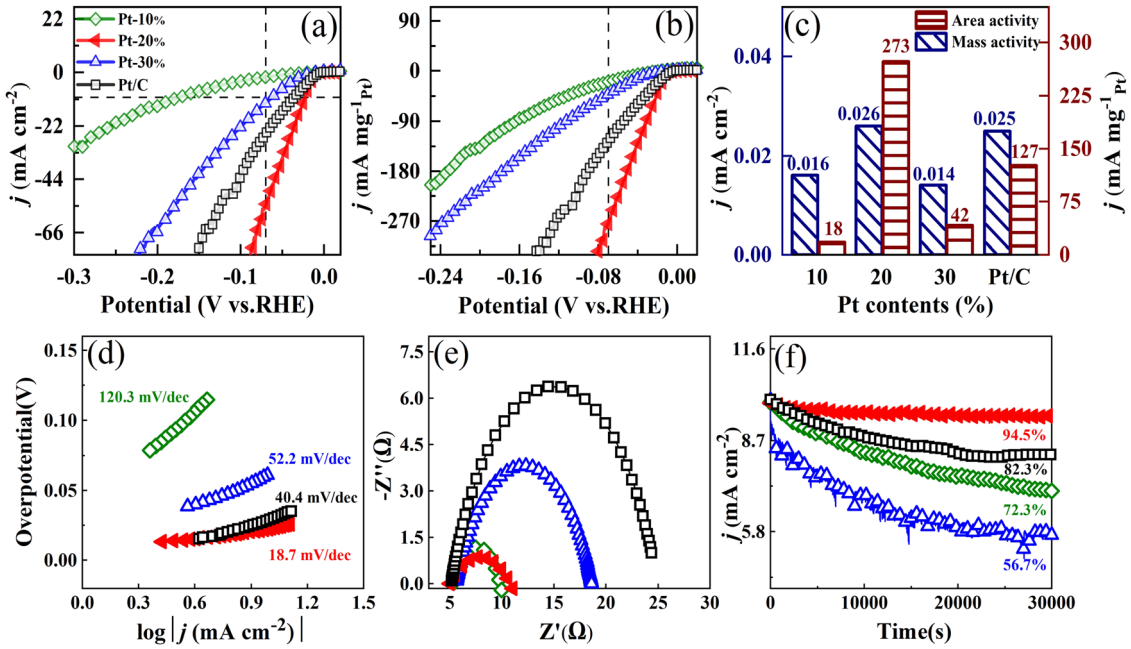

Fig. 7 LSV curves of FeCoNiCuPt HEA NPs with different Pt contents normalized by ECSA (a) and Pt loading (b). (c) Area and mass activity of HEA NPs at −0.07 V. Tafel slopes (d), electrochemical impedance spectroscopy (e), and stability test (f) of HEA NPs. The symbols for different FeCoNiCuPt HEA NPs are consistent, as shown in Fig. 7(a).

These entropies are higher than 1.5R and can be treated as HEA. The maximum entropy is achieved when the FeCoNiCuPt HEA NPs are in nearly equal atomic ratio (20%), which presents the best thermodynamic stability and HER durability.[12,31] The FeCoNiCuPt HEA NPs prepared by the solid-state reaction method present promising applications for electro-catalyzing of the HER in an alkaline environment, the activity and stability of NPs are higher than that of commercial Pt/C when the Pt content is about 20%.

Fig. 8(a) and (b) show the ECSA and Pt loading normalized cyclic voltammetry curves of FeCoNiCuPt HEA NPs in the MOR test. Two oxidation peaks of MOR can be found in the curves; the forward scan peak is located at about 0.9 V and the reverse scan peak is located at about 0.7 V (*vs.* RHE). The current ratios

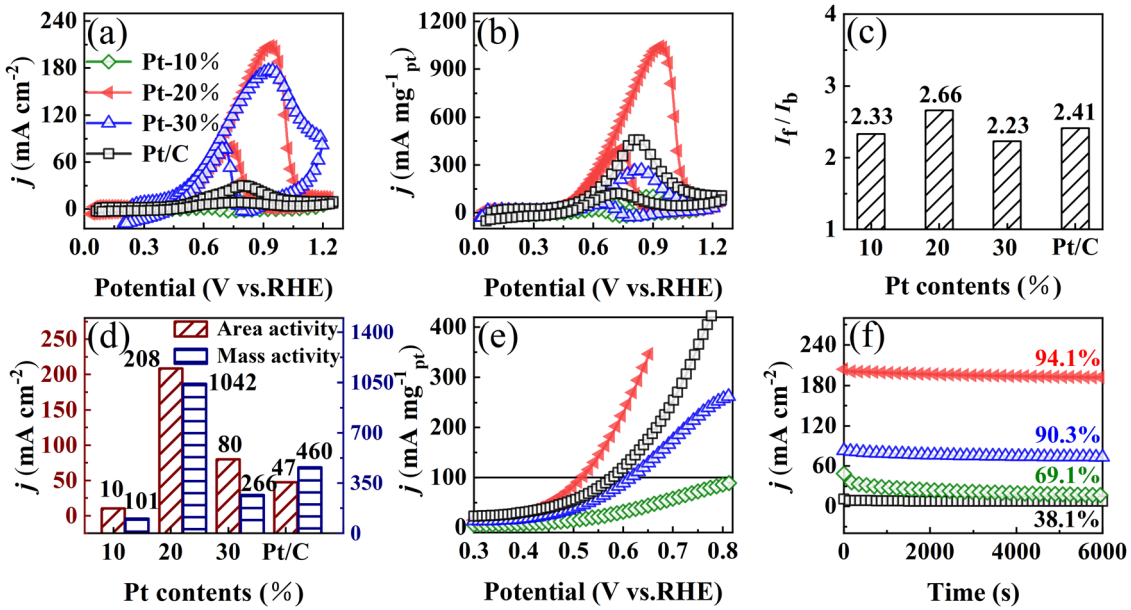

Fig. 8 Cyclic voltammetry curve of FeCoNiCuPt HEA NPs with different Pt content normalized by ECSA (a) and Pt loading (b). (c) The peak current density ratio of forward scanning to backward scanning. (d) Area and mass activity of HEA NPs at peak potential. (e) LSV curve of the catalyst and stability test (f) of HEA NPs. The symbols for different FeCoNiCuPt HEA NPs are consistent, as shown in Fig. 8(a).

(I_f/I_b) of forward scan peak (I_f) to reverse scan peak (I_b) can be used to investigate the tolerance of the NPs to CO. As shown in Fig. 8(c), the current ratio of HEA NPs with 20% Pt content (2.66) is higher than that of Pt/C (2.41); it shows better resistance to CO poisoning. The area and mass activities of HEA NPs at peak potential are summarized in Fig. 8(d). The area activity of HEA NPs is higher than that of Pt/C when the Pt content is 20% and 30%, while the mass activity of HEA NPs is higher than that of Pt/C when the Pt content is 20%. The maximum area activity of 208 mA cm^{-2} and the maximum mass activity of 1042 mA mg_{pt}^{-1} is achieved when the Pt content in HEA NPs is 20%, which are 4.4 and 2.2 times that of commercial Pt/C catalyst (47 mA cm^{-2} and 460 mA mg_{pt}^{-1}). Fig. 8(e) is the LSV curves of FeCoNiCuPt HEA NPs, which can evaluate the MOR difficulty of NPs by the initial overpotential. The overpotentials of HEA NPs with different Pt contents at 100 mA mg_{Pt}^{-1} are 0.818, 0.518, and 0.628 V, respectively. The HEA NPs with 20% Pt content show a lower overpotential, which is only about 89% of commercial Pt/C catalysts (0.582 V). The MOR long-term stability of HEA NPs was tested by chronoamperometry and shown in Fig. 8(f). Due to the accumulation of CO and other intermediates, the current density of the NPs decreased to a certain extent with increasing test time. After 6000 s, the FeCoNiCuPt HEA NPs with Pt content of 10%, 20%, and 30% remain at 69.1%, 94.1%, and 90.3%, respectively. The stability of HEA NPs is higher than that of Pt/C (38.1%) because the alloying elements Fe, Co, Ni, and Cu can facilitate the desorption and transfer of MOR intermediates. The HEA NPs with Pt content of 20% present the best stability toward MOR; it only decreases by about 5.9%. The FeCoNiCuPt HEA NPs prepared by the solid-state reaction method present excellent properties in the electro-catalysis of MOR in an alkaline environment; the activity and stability of NPs reach much higher than that of commercial Pt/C when the Pt content is about 20%. The electrocatalytic HER performance of FeCoNiCuPt HEA NPs synthesized by NaCl-assisted solid-state reaction method are not outstanding as some HEA NPs prepared by low-temperature oil phase strategy or other methods present much better electrocatalytic performance toward HER and MOR,[12–16] which may be caused by the simple technology, preparation, and testing of the electrocatalytic electrode. Nevertheless, the electrocatalytic performances of FeCoNiCuPt HEA NPs are much better than that of Pt/C under the same testing conditions. It is well worth looking forward to obtain excellent performance by the further optimization of the solid-state reaction processes and electrocatalytic electrodes.

3.3 Electronic structure analysis and discussion

Fig. 9(a) shows the top view from the (111) surface of FeCoNiCuPt HEA NPs. The atom ratios of (Fe + Co + Ni + Cu) : Pt in HEA NPs were set as 9 : 1, 8 : 2, and 7 : 3, and the Fe, Co, Ni, and Cu atoms were in equal proportion. These components are not only close to the experimental results but also suitable for analyzing the electronic structure and properties of Pt-based

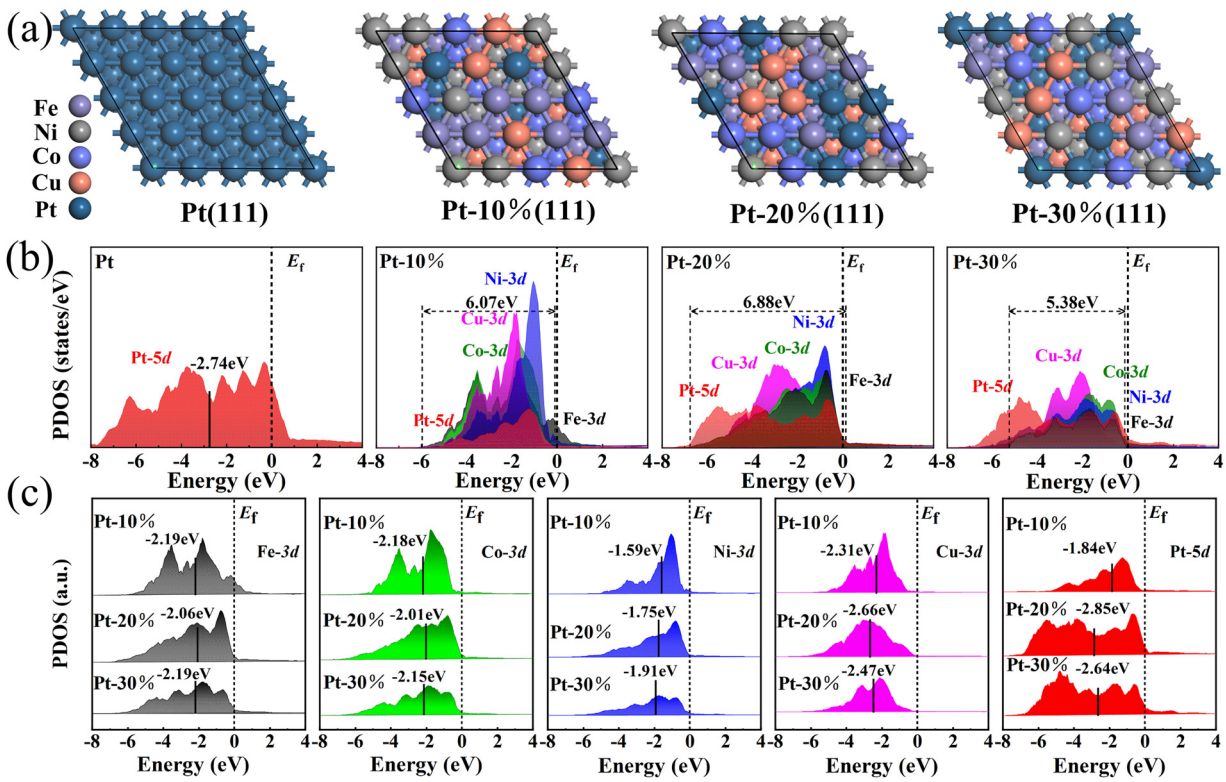

Fig. 9 (a) Top view from the (111) surface of FeCoNiCuPt HEA NPs. (b) PDOS of FeCoNiCuPt HEA NPs with different Pt contents. (c) The Pt content-dependent PDOS and d-band center of Fe, Co, Ni, Cu, and Pt atoms.

HEA NPs. The low-indexed (111) faces of Pt-based fcc structure alloys always present lower surface energy, which is the main part of the exposed surfaces. Covering the (111) face can reduce the total energy of NPs and plays an irreplaceable role in electrocatalysis.[12,17] The atomic arrangement in the (111) surface of HEA NPs is constructed by the ATAT (mcsqs) method and geometric optimization, in which the energy of NPs is the most stable.[15–17] As the high solid-state reaction temperature, these models are the most appropriate. As the HER or MOR reaction pathways of FeCoNiCuPt HEA NPs have already been revealed by Li,[12] the electronic structure differences of FeCoNiCuPt HEA NPs with respect to different Pt content are studied in this research.

The projected density of states (PDOS) distributions of Pt and FeCoNiCuPt HEA NPs are shown in Fig. 9(b). The d orbital of Fe, Co, Ni, Cu, and Pt atoms play a leading role in the HER electrocatalytic process. The energy distribution of the Pt-5d orbital becomes more uniform and moves to the left side when alloying with Fe, Co, Ni, and Cu atoms, which means that the strong adsorption of Pt is reduced.[10–12] In HEA NPs, the Pt 5d orbital is far away from the Fermi level (E_V = 0 eV), which acts as an electron reservoir for the reduction process, such as the transfer of electrons in HER and OH^- in MOR. The Ni 3d and Fe 3d orbitals dominate near the Fermi level, providing an electron depletion center for HER and MOR. The 3d orbitals of Co and Cu are located between Pt 5d and Ni/Fe 3d, which acts as the bridge of electron transfer and can reduce the energy barrier of intermediates transfer in the HER and MOR process.[9–12] The overlap of Pt 5d and Fe/Co/Ni/Cu 3d orbitals suggests the good conductivity and catalytic activity of HEA NPs. The overlap bandwidth of 10%, 20%, and 30% HEA NPs is 6.07, 6.88, and 5.38 eV, receptivity. The maximum overlap bandwidth is reached when the Pt content is 20%, which means that the coordination of the elements in the HER electrocatalytic process is the best.[9–12] In addition, the narrow Fe/Co/Ni/Cu 3d orbitals become weak when the Pt content in FeCoNiCuPt HEA NPs is higher than 10%. Both the overlap and shape of orbitals illustrate that the cocktail effect of each element is the strongest when the Pt content is 20%,[9–12] which means that the active sites on the surface of NPs are the most and the ECSA of HEA NPs is the maximum. The overlap bandwidth of HEA NPs is decreased when the Pt content increases to 30%, which leads to a reduction of ECSA. With lower Pt content and poorer interaction of d orbitals from each element, the ECSA of 10% Pt content HEA NPs is the minimum, although the HEA NPs obtain the smallest size.

Both experimental and DFT calculation method illustrates that the 20% Pt content HEA NPs presents the best HER electrocatalytic activity. It must be noticed that the size of FeCoNiCuPt HEA NPs is increased with the increase in the Pt content. The HEA NPs with 10% Pt content shows the minimum size, but the ECSA and electrocatalytic activity is smaller than that of 20% Pt content HEA NPs and the commercial Pt/C catalyst.[19,20] Otherwise, in view of lattice mismatch, the stress in FeCoNiCuPt HEA NPs is increased with larger Pt atoms, but the electrocatalytic activity is smaller than that of 20% Pt content HEA NPs.[10,11] These differences may have originated from the electron structure of HEA NPs with various Pt contents. With the increasing Pt content in FeCoNiCuPt HEA NPs, the evolutions of the d-band center from each element are shown in Fig. 9(c). The PDOS of the Fe 3d orbital moves to the left side of the Fermi level, which means that the strong adsorption of Fe is weakened when the Pt content is higher than 10%.[9–12] The d-band center of Fe 3d moves to close the Fermi level only when the Pt content is 20%, which reveals that the electron depletion for the HER and MOR processes is enhanced. The d-band center of the Co 3d orbital right shifts with increasing Pt content in HEA NPs; the right shift is the largest when the Pt content is 20%. The d-band center of the Ni 3d orbital left shifts with the increase in the Pt content in HEA NPs, which is unfavorable to electron depletion of the HER and MOR processes. The lower charge transfer resistance (from EIS) of HEA NPs when the Pt content is 10% and 20%, which may be originated from the electron depletion of Fe, Co, and Ni atoms. Although the electron depletion of Ni is weakened when the Pt content is 20%, the electron depletion of Fe and Co atoms is enhanced. The d-band center of Cu 3d moves to the left side with increasing Pt content in HEA NPs, closer to the d-band center of Pt 5d, which facilitates the electron transfer process. The d-band center of Pt 5d moves to the left side with increasing Pt content in HEA NPs, which means that the electron reservoir of Pt is enhanced. However, the d-band center of Pt 5d is lower than Pt only when the Pt content is 20%. As the lowest d-band center of Pt 5d enhances most of the electron reservoir, the Fe, Co, and Ni atoms lower the charge transfer resistance by improving electron depletion, and the Cu atoms facilitate the electron transfer, the coordinate effects of each element reach the best, and the maximum HER and MOR activity is obtained when the Pt content in FeCoNiCuPt HEA NPs is 20%.

4. Conclusion

The FeCoNiCuPt HEA NPs with smaller sizes (3–7 nm) and different Pt contents were successfully synthesized by the solid-state reaction method. The exposed surface absorbing or oxidation of Fe, Co, Ni, and Cu elements, the centered diffraction angles of a single solid solution phase with fcc structure, and the uniform elemental distributions in the nanoparticles illustrate the HEA characteristic of NPs. Increasing the Pt content in HEA NPs from 10% to 30%, the lattice parameter was increased because the radius of Pt atoms is larger, and the grain size was increased with decreasing nucleation ratio. The overlap of Pt 5d and Fe/Co/Ni/Cu 3d orbitals became weak when the Pt contents were 20% and 30%, which increased the C_{dl} and ESCA of HEA NPs to higher than that of commercial Pt/C catalysts. When the Pt content in FeCoNiCuPt HEA NPs was 20%, the lowest d-band center of Pt 5d enhanced most of the electron reservoir, the Fe, Co, and Ni atoms lowered the charge transfer resistance by improving electron depletion, and the Cu atoms facilitated electron transfer. As the best coordinate effects of each element and the largest entropy value of 20% Pt content HEA NPs, the

maximum HER activities, MOR activities, and long-term stability were obtained. The electrocatalytic performance of Pt-based HEA NPs could be improved by adjusting the Pt content, which would optimize the electron structure and entropy value of NPs.

Author contributions

Chao Meng and Xuhui Wang: writing – original draft, investigation, formal analysis. Zhiyong Li, Chang Lin and Runqing Liu: investigation, funding acquisition, formal analysis. Chun Wu and Wenli Pei: writing – review & editing, project administration, supervision, funding acquisition.

Conflicts of interest

There are no conflicts to declare.

Acknowledgements

This work was financially supported by the National Key Research and Development Program of China (Grant No. 2021YFB3501404), the National Natural Science Foundation of China (Grant No. 52071070, and 52102360), the China Postdoctoral Science Foundation (Grant No. 2023M732392), the Opening Fund of Key Laboratory of Electromagnetic Processing of Materials (Grant No. NEU-EPM-025), and the Discipline Innovation Team of Liaoning Technical University (Grant No. LNTU20TD-16).

References

1 J. Zhu, Y. Yang, L. Chen, W. Xiao, H. Liu, H. D. Abruna and D. Wang, Copper-induced formation of structurally ordered Pt–Fe–Cu ternary intermetallic electrocatalysts with tunable phase structure and improved stability, *Chem. Mater.*, 2018, **30**, 5987–5995.

2 L. Chen, J. Zhu, C. Xuan, W. Xiao, K. Xia, W. Xia, C. Lai, H. L. Xin and D. Wang, Effects of crystal phase and composition on structurally ordered Pt–Co–Ni/C ternary intermetallic electrocatalysts for the formic acid oxidation reaction, *J. Mater. Chem. A*, 2018, **6**, 5848–5855.

3 S. Wang, Z. Deng, J. Li, H. Liu, Y. Wang and X. Fu, Efficient electrolytic water splitting with FeCoPt trimetallic cubic nanocatalysts, *IOP Conf. Ser.: Mater. Sci. Eng.*, 2019, **592**, 012043.

4 C. Wu, D. Zheng, X. Wang, X. Wang, W. Pei, K. Wang and Q. Wang, Effects of high magnetic field on the growth and magnetic property of $L1_0$-FePtCu nanoparticles, *J. Magn. Magn. Mater.*, 2021, **526**, 167731.

5 C. Wu, Y. Ju, L. Chang, S. Dong, R. Liu, K. Wang, W. Pei and Q. Wang, Magnetic flux density-determined oriented attachment growth of FePt nanowires, *CrystEngComm*, 2022, **24**, 4320–4326.

6 C. Wu, X. Wang, W. Pei, D. Zhao, K. Wang, G. Li and Q. Wang, Tailoring the shape and size of wet-chemical synthesized FePt nanoparticles by controlling nucleation and growth with a high magnetic field, *Nanoscale*, 2019, **11**, 15023–15028.

7 X. Duan, C. Wu, X. Wang, X. Tian, W. Pei, K. Wang and Q. Wang, Evolutions of microstructure and magnetic property of wet-chemical synthesized FePt nanoparticles assisted by high magnetic field, *J. Alloys Compd.*, 2019, **797**, 1372–1377.

8 A. K. Ipadeola, A. K. Lebechi, L. Gaolatlhe, A. B. Haruna, M. Chitt, K. Eid, A. M. Abdullah and K. I. Ozoemena, Porous high-entropy alloys as efficient electrocatalysts for water-splitting reactions, *Electrochem. Commun.*, 2022, **136**, 107207.

9 H. Li, J. Lai, Z. Li and L. Wang, Multi-sites electrocatalysis in high-entropy alloys, *Adv. Funct. Mater.*, 2021, **31**, 2106715.

10 K. Wang, J. Huang, H. Chen, Y. Wang, W. Yan, X. Yuan, S. Song and J. Zhang, Recent progress in high entropy alloys for electrocatalysts, *Electrochem. Energy Rev.*, 2022, **5**, 17.

11 X. Huo, H. Yu, B. Xing, X. Zuo and N. Zhang, Review of high entropy alloys electrocatalysts for hydrogen evolution, oxygen evolution, and oxygen reduction reaction, *Chem. Rec.*, 2022, **22**, e202200175.

12 H. Li, Y. Han, H. Zhao, W. Qi, D. Zhang, Y. Yu, W. Cai, S. Li, J. Lai, B. Huang and L. Wang, Fast site-to-site electron transfer of high-entropy alloy nanocatalyst driving redox electrocatalysis, *Nat. Commun.*, 2020, **11**, 5437.

13 S. Yuan, X. Zhu, H. Li, Z. Hu, Q. Ren, W. Zhao, X. Tang and S. Hu, Ultrathin wavy nanowires of high-entropy alloy as cocktail solution in methanol oxidation reaction, *Prog. Nat. Sci.: Mater. Int.*, 2023, **33**, 225–231.

14 D. Wang, Z. Chen, Y. Huang, W. Li, J. Wang, Z. Lu, K. Gu, T. Wang, Y. Wu, C. Chen and Y. Zhang, Tailoring lattice strain in ultra-fine high-entropy alloys for active and stable methanol oxidation, *Sci. China Mater.*, 2021, **64**, 2454–2466.

15 G. Feng, F. Ning, J. Song, H. Shang, K. Zhang, Z. Ding, P. Gao, W. Chu and D. Xia, Sub-2 nm ultrasmall high-entropy alloy nanoparticles for extremely superior electrocatalytic hydrogen evolution, *J. Am. Chem. Soc.*, 2021, **143**, 17117–17127.

16 H. Chen, C. Guan and H. Feng, Pt-based high-entropy alloy nanoparticles as bifunctional electrocatalysts for hydrogen and oxygen evolution, *ACS Appl. Nano Mater.*, 2022, **5**, 9810–9817.

17 D. S. R. Rocabado, Y. Nanba and M. Koyama, Electronic structure and phase stability of Pt_3M (M = Co, Ni, and Cu) bimetallic nanoparticles, *Comput. Mater. Sci.*, 2020, **184**, 10984.

18 L. Bai, S. Zhang, Q. Chen and C. Gao, Synthesis of ultrasmall platinum nanoparticles on polymer nanoshells for size-dependent catalytic oxidation reactions, *ACS Appl. Mater. Interfaces*, 2017, **9**, 9710–9717.

19 L. Gan, S. Rudi, C. Cui, M. Heggen and P. Strasser, Size-controlled synthesis of sub-10 nm $PtNi_3$ alloy nanoparticles and their unusual volcano-shaped size effect on ORR electrocatalysis, *Small*, 2016, **12**, 3189–3196.

20 T. Wang, J. Liang, Z. Zhao, S. Li, G. Lu, Z. Xia, C. Wang, J. Luo, J. Han, C. Ma, Y. Huang and Q. Li, Sub-6 nm fully

ordered $L1_0$-Pt–Ni–Co nanoparticles enhance oxygen reduction via Co doping induced ferromagnetism enhancement and optimized surface strain, *Adv. Energy Mater.*, 2019, **9**, 1803771.

21 J. Yan, Y. Wang, Y. Zhang, S. Xia, J. Yu and B. Ding, Direct magnetic reinforcement of electrocatalytic ORR/OER with electromagnetic induction of magnetic catalysts, *Adv. Mater.*, 2021, **33**, e2007525.

22 F. Lu, J. Wang, J. Li, Y. Du, X. P. Kong, S. Liu, D. Yi, Y. K. Takahashi, K. Hono, X. Wang and J. Yao, Regulation of oxygen reduction reaction by the magnetic effect of $L1_0$-PtFe alloy, *Appl. Catal., B*, 2020, **278**, 119332.

23 J. Liang, Z. Zhao, N. Li, X. Wang, S. Li, X. Liu, T. Wang, G. Lu, D. Wang, B. Joe Hwang, Y. Huang, D. Su and Q. Li, Biaxial strains mediated oxygen reduction electrocatalysis on Fenton reaction resistant $L1_0$-PtZn fuel cell cathode, *Adv. Energy Mater.*, 2020, **10**, 2000179.

24 J. He, B. Bian, Q. Zheng, J. Du, W. Xia, J. Zhang, A. Yan and J. P. Liu, Direct chemical synthesis of well dispersed $L1_0$-FePt nanoparticles with tunable size and coercivity, *Green Chem.*, 2016, **18**, 417–422.

25 S. Dong, Y. Ju, Y. Jiang, C. Meng, R. Liu, C. Wu and W. Pei, Effects of solid isolation medium on the microstructure and magnetic properties of one-step sintered $L1_0$-FePtCu nanoparticles, *J. Alloys Compd.*, 2022, **909**, 164748.

26 D. Zhao, X. Wang, L. Chang, W. Pei, C. Wu, F. Wang, L. Zhang, J. Wang and Q. Wang, Synthesis of super-fine $L1_0$-FePt nanoparticles with high ordering degree by two-step sintering under high magnetic field, *J. Mater. Sci. Technol.*, 2021, **73**, 178–185.

27 W. Pei, D. Zhao, C. Wu, X. Wang, K. Wang, J. Wang and Q. Wang, Facile liquid-assisted one-step sintering synthesis of superfine $L1_0$-FePt nanoparticles, *RSC Adv.*, 2019, **9**, 36034–36039.

28 B. Jiang, Y. Guo, F. Sun and S. Wang, *et al.*, Nanoarchitectonics of metallene materials for electrocatalysis, *ACS Nano*, 2023, **17**, 13017–13043.

29 S. Wang, B. Xu, W. Huo, H. Feng, X. Zhou, F. Fang, Z. Xie, J. K. Shang and J. Jiang, Efficient FeCoNiCuPd thin-film electrocatalyst for alkaline oxygen and hydrogen evolution reactions, *Appl. Catal., B*, 2022, **313**, 121472.

30 D. Feng, Y. Dong, P. Nie, L. Zhang and Z. A. Qiao, CoNiCuMgZn high entropy alloy nanoparticles embedded onto graphene sheets via anchoring and alloying strategy as efficient electrocatalysts for hydrogen evolution reaction, *Chem. Eng. J.*, 2022, **430**, 132883.

31 T. Chen, F. Ning, J. Qi, G. Feng, Y. Wang, J. Song, T. Yang, X. Liu, L. Chen and D. Xia, PtFeCoNiCu high-entropy solid solution alloy as highly efficient electrocatalyst for the oxygen reduction reaction, *iScience*, 2023, **26**, 105890.

32 J. Lai and S. Guo, Design of ultrathin Pt-based multimetallic nanostructures for efficient oxygen reduction electrocatalysis, *Small*, 2017, **13**, 1702156.

33 S. Grimme, J. Antony, S. Ehrlich and H. Krieg, A consistent and accurate ab initio parametrization of density functional dispersion correction (DFT-D) for the 94 elements H-Pu, *J. Chem. Phys.*, 2010, **132**, 154104.

34 X. Huang, G. Yang, S. Li, H. Wang, Y. Cao, F. Peng and H. Yu, Noble-metal-based high-entropy-alloy nanoparticles for electrocatalysis, *J. Energy Chem.*, 2022, **68**, 721–751.

35 A. I. Inamdar, H. S. Chavan, B. Hou, C. H. Lee, S. U. Lee, S. N. Cha, H. Kim and H. Im, A robust nonprecious CuFe composite as a highly efficient bifunctional catalyst for overall electrochemical water splitting, *Small*, 2020, **16**, e1905884.

36 W. Shi, H. Liu, Z. Li, C. Li, J. Zhou, Y. Yuan, F. Jiang, K. Fu and Y. Yao, High-entropy alloy stabilized and activated Pt clusters for highly efficient electrocatalysis, *SusMat*, 2022, **2**, 186–196.

37 A. Sivanantham, H. Lee, S. W. Hwang, B. Ahn and I. S. Cho, Preparation, electrical and electrochemical characterizations of CuCoNiFeMn high-entropy-alloy for overall water splitting at neutral-pH, *J. Mater. Chem. A*, 2021, **9**, 16841–16851.

38 C. Wan, G. Li, J. Wang and L. Xu, *et al.*, Modulating Electronic Metal-Support Interactions to Boost Visible-Light-Driven Hydrolysis of Ammonia Borane: Nickel-Platinum Nanoparticles Supported on Phosphorus-Doped Titania, *Angew. Chem., Int. Ed.*, 2023, **62**, e202305371.

39 Y. Kang, O. Cretu, J. Kikkawa and K. Kimoto, Mesoporous multimetallic nanospheres with exposed highly entropic alloy sites, *Nat. Commun.*, 2023, **14**, 4182.

40 Z. X. Cai, Z. L. Wang, Y. J. Xia and H. Lim, *et al.*, Tailored catalytic nanoframes from metal–organic frameworks by anisotropic surface modification and etching for the hydrogen evolution reaction, *Angew. Chem.*, 2021, **133**, 4797–4805.

41 Z. Jia, K. Nomoto, Q. Wang, C. Kong, L. Sun, L. C. Zhang, S. X. Liang, J. Lu and J. J. Kruzic, A self-supported high-entropy metallic glass with a nanosponge architecture for efficient hydrogen evolution under alkaline and acidic conditions, *Adv. Funct. Mater.*, 2021, **31**, 2101586.